A Tunable 3D Printed Microfluidic Resistive Pulse Sensor for the Characterisation of Algae and Microplastics

Mark Platt, Eugenie Hunsicker, Marcus Pollard

Technologies that can detect and characterise particulates in liquids have applications in health, food and environmental monitoring. Here we present a low-cost and high-throughput multiuse counter that classifies a particle's size, concentration, porosity and shape. Using an additive manufacturing process, we have assembled a reusable flow resistive pulse sensor. The device remains stable for several days with repeat measurements. We demonstrate its use for characterising algae with spherical and rod structures as well as microplastics shed from teabags. We present a methodology that results in a specific signal for microplastics, namely a conductive pulse, in contrast to particles with smooth surfaces such as calibration particles or algae, allowing the presence of microplastics to be easily confirmed and quantified. In addition, the shape of the signal and particle are correlated, giving an extra physical property to characterise suspended particulates. The technology can rapidly screen volumes of liquid, 1 mL/ min, for the presence of microplastics and algae.

File list (1)

Additively Manufactured Tuneable Flow Resistive Pulse ... (878.46 KiB)   view on ChemRxiv • download file

A Tunable 3D Printed Microfluidic Resistive Pulse Sensor for the Characterisation of Algae and Microplastics.

M. Pollard,[1] E. Hunsicker,[1] M. Platt[1*]

1 – School of Science, Loughborough University. Epinal Way. LE11 3TU

* Corresponding author m.platt@lboro.ac.uk

Abstract

Technologies that can detect and characterise particulates in liquids have applications in health, food and environmental monitoring. Simply counting the numbers of cells or particles however is not sufficient for most applications, and other physical properties must also be measured. Typically, it is necessary to compromise between chemical and biological specificity of the sensor and its speed. Here we present a low-cost and high-throughput multiuse counter that classifies a particle's size, concentration, porosity and shape. Using an additive manufacturing process, we have assembled a reusable flow resistive pulse sensor capable of being be tuned in real time to measure particles from $2 - 30$ μm, across a range of salt concentrations i.e. 2.5×10^{-4} to 0.1M. The device remains stable for several days with repeat measurements. We demonstrate its use for characterising algae with spherical and rod structures as well as microplastics shed from teabags. We present a methodology that results in a specific signal for microplastics, namely a conductive pulse, in contrast to particles with smooth surfaces such as calibration particles or algae, allowing the presence of microplastics to be easily confirmed and quantified. In addition, the shape of the signal and particle are correlated, giving an extra physical property to characterise suspended particulates. The technology can rapidly screen volumes of liquid, 1 mL/ min, for the presence of microplastics and algae.

Keywords: Resistive Pulse Sensor, Micro plastic, Algae, Environmental, Food.

Introduction:

Monitoring the presence of particles, be they biological or manmade, within the environment requires a multidisciplinary approach. Microplastics are an increasing cause of concern due to their ubiquity, and their impact within the food chain and upon health is poorly understood. Algae communities are a good indicator species that are sensitive to changes in their habitat. The total biomass of algae and their diversity can be used as indicators of water quality, which makes them a universal indicator species. New analytical technologies can aid the characterisation of algae quickly regardless of solution properties, salt levels and turbidity. Whilst current methods can monitor the presence of algae remotely by buoy in-takes,[1–3] or via satellite imaging to track algal blooms,[4] these methods are unable to differentiate and quantify biological and manmade particulates.

Resistive Pulse Sensors (RPS), based upon the Coulter Counter principle have seen a resurgence in the last two decades. When integrated into microfluidic systems, this 1950's technology is finding new applications.[5–9] New manufacturing processes, coupled with improved electronics have enabled them to characterise analytes' sizes[10–12], concentrations[13,14], shapes[15] and charges.[16,17] As a result, RPS has found numerous applications within environmental monitoring of, for example: bacteria[18], algae[19], and heavy metal ions[20]. The sensing system is simple, monitoring the temporary changes in current caused by the translocation of an analyte through a narrow constriction, termed a sensing region. Their limited number of components make them easy to manufacture, requiring only two electrodes, a constriction and a solution containing an electrolyte in order for the sensor to operate. The key aspects which determine the sensitivity in these devices are the sensing regions dimensions, as the signal generated by the analyte is proportional to the volume of the sensing region it excludes. A smaller sensing region can detect smaller analytes, however creating the smaller sensing regions requires advanced manufacturing processes, and they can lead to blockages when larger analytes or aggregates are present.

Additive manufacturing (AM), or 3D printing, has recently gained considerable attention as an alternative to traditional lithography. This method of fabrication allows three dimensional devices to be rapidly produced. One of the most popular types of additive manufacturing is stereolithography (SLA).[21–23] Here the device is produced layer by layer by exposing a photosensitive polymer to UV light, causing it to cure before a new layer is formed. This produces devices which are water tight with high resolution features using low cost printers[24]. The limitation to the feature size is dependent on the pixel or laser spot size as this determines the minimum curable area.[21,23] One aspect that stereolithography struggles with is producing microfluidic devices with internal voids or channels. Once these are printed, the resin needs to be flushed out of the void before it is usable. Also over-curing, when the UV light causes resin within the channel to cure, can cause a channel to seal.[24] Therefore many AM microfluidics have featured channel sizes exceeding 0.5 mm[25,26]. Recently, Gong et al demonstrated a custom 3D printer which was capable of printing channels with a cross section of 18 x 20 microns which is an encouraging sign for AM produced microfluidics.

Whilst 2-photon polymerisation offers an opportunity to print smaller channels[24,27,28], the integration of these into higher throughput flow systems has yet to be demonstrated.

We have previously used surface channels within AM devices sealed with a polymer acetate film to overcome the issue of channel blockage, termed gen 1 in this study. Using this method, commercial SLA printers and resins could reproducibility produce channels ≥ 100 μm, which were used as a gen-1 flow-RPS device.[29] However, a drawback of this process was the lifetime of the device, as over longer periods e.g. 24 hours, the adhesive on the polymer film weakened, causing it to peel off, or encroach into the channel, blocking it. Here we overcome these issues and extend the sensing dynamic range to smaller particles. The second generation device has been created with a re-sealable easy to change lid and a compressible Polydimethylsiloxane (PDMS) gasket layer that extends the sensing range to detect particles below 5μm. The device uses a lid which is held in place via screws, between the base unit and lid sits the PDMS layer. When the screws are tightened, the lid is pushed into the sensing region, reducing the dimensions of the sensing region and increasing the size sensitivity of the device. The lids can be easily interchanged with no modification to the flow device base, meaning in the event of blockage or damage, the lid can be removed the device and cleaned, or the lid replaced with minimal downtime. Here we use the device to characterise size, concentration, and, unique to this study the porosity of microplastics and shape classification of two strains of algae.

Experimental

Chemicals and reagents: CPC2000, 2 micron carboxylated polystyrene calibration particles were obtained from Izon Science Ltd, 10 micron and 20 micron carboxlyated polystyrene calibration particles denoted as CP10M and CP20M were obtained from Izon Science Ltd. 30 Micron carboxylated polystyrene particles, Cat No. 84135, were obtained from Sigma-Aldrich, potassium chloride obtained from Fisher Scientific UK, >99% cat no: P/4240/60, Acc Silicones QSil216 was obtained from RS components, catalogue no: 458-765, part no: QSil 216, Algae samples were obtained from Roscoff Culture Collection, *Aurantiochytrium Mangrovei* (Spherical)*,* catalogue number: RCC893 and *Navicula ramosissima* (Rod), catalogue number: RCC5374, Isopropanol obtained from VWR.

Data Analysis: Data analysis was performed within the data analysis module of the Izon control suite, baseline extraction was performed using molecular devices clampfit version 10.7, and pulse shape analysis was performed with a custom R Code.

Device Assembly: In order to assemble the device, the lid was affixed to the base via six machine screws, figure 1, located at each corner, and two screws in the middle of the device. The screws were tightened and secured in place using nuts. Into each one of the screw threads, HPLC fittings were attached in order to accommodate the inlet from the pumps, the electrodes and the outlet. Once fully assembled, the device was

placed into a custom-made faraday cage and electrolyte solution was pumped into the device.

Device Printing: Both the lid and base of the device were printed on an Asiga Pico HD27 UV using FORMlabs clear resin. Files were converted from the CAD software, Siemens NX11 to STL and prepared for printing using Asiga Composer software. Once printed, the parts were cleaned and post cured using a UV light box.

PDMS Gasket: The PDMS gaskets were formed by mixing parts A and B of QSil 216 in a 10:1 ratio. The lid was placed into a petri dish with the ridge oriented to the bottom. The uncured PDMS was poured around the edge of the lid making sure that the whole lid was covered up the ridge and no larger air pockets remained. The PDMS was then cured for one hour at 70°C or until set.

SEM/EDS and Optical Imaging: Prior to SEM imaging, the samples were sputter coated in Au/Pd for 90 seconds using a Quorum Q150T ES gold sputter coater. SEM images were captured on a Zeiss 1530VP FEGSEM. EDS data was captured using Oxford instruments X-mas $80mm^2$ detector and processed using Oxford Instruments Aztec EDS microanalysis software. Microscope images were captured using a Nixon Optiphot 2 optical microscope, and images were captured using a DS 5M camera with a DS-L1 camera control unit.

Electrode fabrication: Electrodes were fabricated by inserting a section of silver wire, 0.25 mm diameter, 99.99% purity obtained from Advent Research materials catalogue no: AG5485, into a pipette tip. A small section of the wire is threaded through the narrow end of the pipette, and the wire is glued in place using Araldite® Rapid epoxy resin; the electrodes were then left to dry.

Sample run: Samples were loaded into Dolomite mitos p-pump which is controlled via flow control centre software. Once the required pressure has been entered into the software, the pumps then drive the sample into the device. When signals are detected, the recording software is activated and each sample is recorded for the required time or until the required number of particles have been detected. The flow rate was determined by setting the lid to the required baseline and pressure. A pre-weighed Eppendorf was then positioned at the outlet for one minute, then removed and reweighed to determine the mass and volume of the liquid run through the device over that period of time.

Tea sample preparation: Tea samples were prepared by making an incision into the bag and discarding the contents. The bags were then washed with deionised water and allowed to dry. Finally, a glass vial of deionised water was heated to 95°C and the dried tea bag was placed into the vial for 5 minutes. After 5 minutes, the solution was decanted into another vial and allowed to cool. The sample was then diluted to the required concentration with electrolyte solution.

Tea sample electron microscopy preparation: The samples were prepared by vacuum filtrating the decanted solution using an ANODISK 47 mm filtration membrane, 0.02 micron. The membrane was then washed five times with deionised water, 15 MΩ, and allowed to dry before being mounted onto an aluminium SEM stub using a carbon adhesive tab.

Pulse shape analysis: The pulses were analysed by custom R code which has been previously reported[15]. Pulses were extracted, detrended and aligned, then approximated using b-splines (using the COBS package). Logistic models for shape/run discrimination were built on training data using three spline coefficients showing the greatest predictive power for shape classification (under lasso penalised regression using the glmnet package). Classification power was then evaluated on independent testing data.

Results

Figure 1a-d, shows images of the base unit, lid, sensing zone and electrodes. The lids can have several designs; the first is a flat surface that mimics the acetate film from gen 1. The second design has a ridge that extends 1 mm out from the surface and is aligned to extend into the channel. The third has multiple ridges that can change the shape of channel and sensing region, figure 1e. The device was designed to be integrated into a flow system, thus has printed screw threads to connect pumps. As well as the lid design, a second alteration from gen 1 is the integration of the electrodes' screw threads, see figure 1d. Figure s1 shows all the dimensions and photographs of the components.
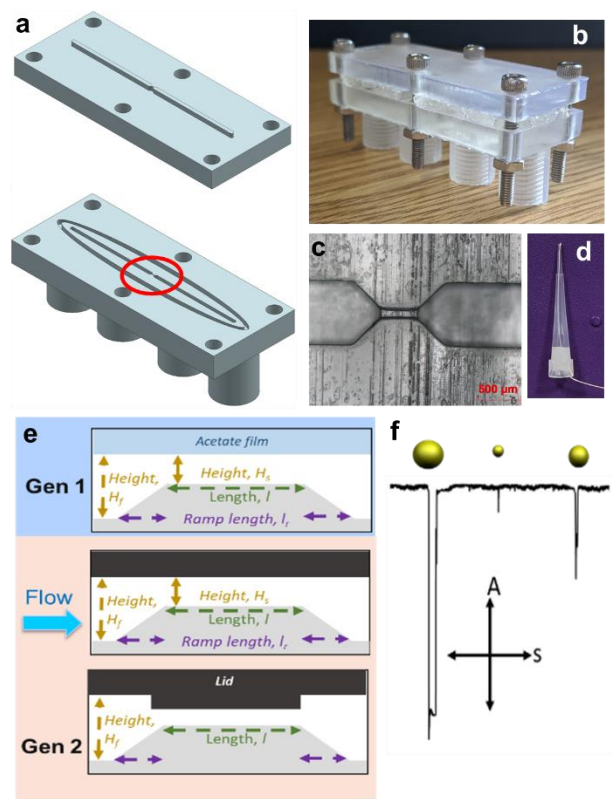
Figure 1 a) CAD design of the device, b) Image of the assembled device, c) an optical microscope image of the sensing zones circled in part a, d) silver wire embedded within a pipette tip, e) schematic of the sensing zone when using an acetate film, a flat lid and ridge lid, f) schematic of the resistive pulses expected when a particle passes through the sensing zone.

Optical images of the channel, ridge lid and PDMS layer are shown in figure 2a. The PDMS layer acts as a gasket sealing the components and preventing any leakage. It is held in place by the screws, and the shape or dimensions (internal volume) of the channel can be controlled via two mechanisms. The first is by altering the shape and structures on the lid. As show in figure 1, the lid can be made with a flat surface, or containing protrusions designed to fit within the main channel in base unit. The second option is to use the PDMS layer, which is compressed into the channel upon the application of a force via the screws. Figure 2 shows the schematic of this process, for the flat lid the PDMS covers its entire under surface and as the screw tension is increased, it forces the flexible PDMS gasket into the channel, causing the channel's internal volume to decrease. For the second lid design, the ridge causes the largest change in channel volume upon tightening of the screws, as opposed to the PDMS layer, which does not extent over the ridge itself.
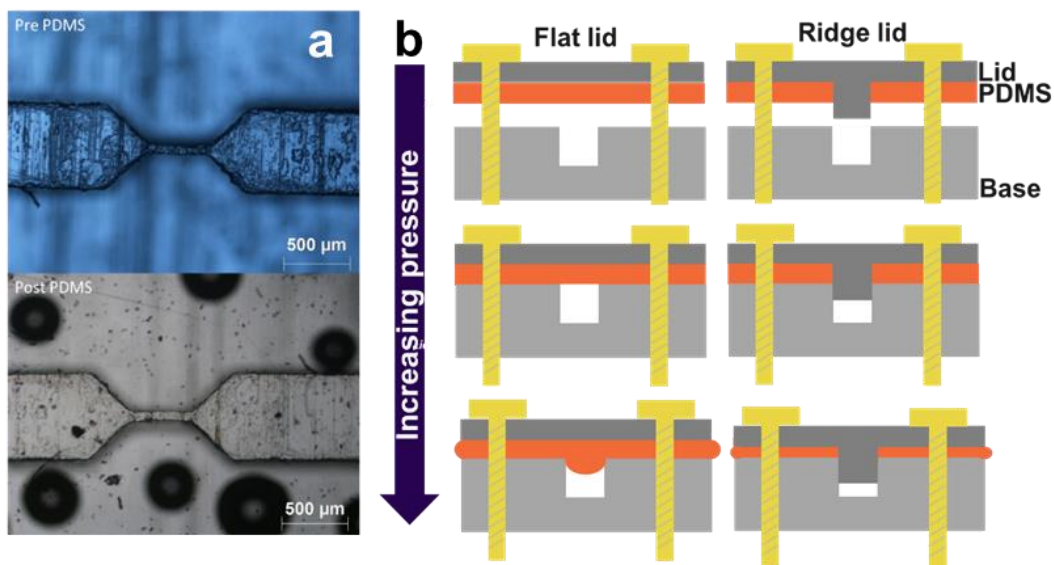

Figure 2a) Optical images of the ridge lid before and after a PDMS coating. b) Schematic of the sealed device with two lid designs.

When the channel is filled with a conductive liquid and a potential difference is applied between the two electrodes, the size of the channel can be monitored in real time through the base line current, I, as I is proportional to the sensing volume using the equation 1 the resistance can then be related to the current via Ohm's law[30]:

$$R = L/\sigma hw, \qquad (1)$$

where R is the resistance, L is the channel length, σ is conductivity of solution, and h and w are the height and width of the channel, respectively. Figure 3a shows the flow rate versus baseline current for the flat lid device under a constant applied pump

pressure. The base line current was controlled by changing the pressure on the lid through the screws. A higher force, compressed the PDMS layer or ridge further into the channel and resulted in a smaller base line current. The data in figure 3a shows the relationship between base line current and screw tension, illustrating the use of a compressible PDMS layer to tune the channel dimensions. Figure s2 shows the measured flow rate versus applied pump pressure for different channel dimensions. By adding a ridge on the lid that extends into the flow, the shape of the sensing region as well as its internal volume is reduced further, figure 2b. The screws and PDMS compression layer allow further tuning of the channel volume. An extreme version of this allows the ridge to fully seal the channel and acts like a 3D printed valve illustrated elsewhere[31,32], data not shown.
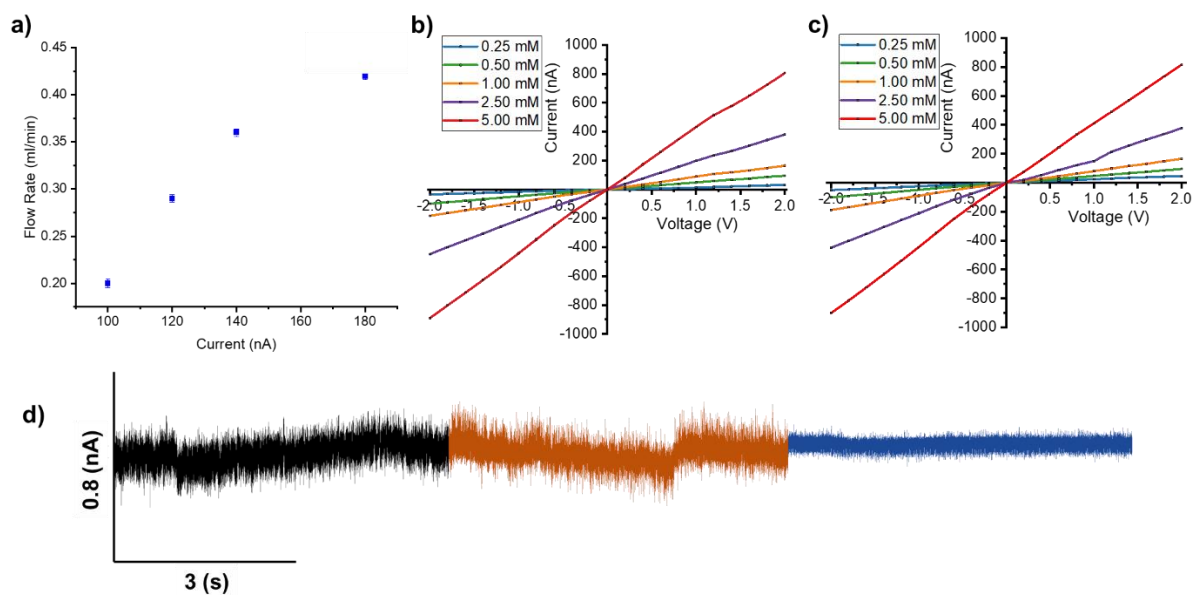

Figure 3. a) Plot of measured current versus flow rate for a flat PDMS lid, voltage = 5.64 V, 0.25 mM KCl. Current-Voltage plots for b) Absence of flow c) 100 mbar of pressure applied to the liquid, d) Baseline currents for the device with 100 mbar flow pressure in 100, 50 and 0.25 mM KCl (left to right), Voltage = 0.5V (100mM), 0.6V (50 mM), 8.5V (0.25mM).

Figure 3 also illustrates the relationship between applied voltage and current for the ridge lid in the presence and absence of convection. The linear relationship between current-voltage and the consistency of the current in the presence of fluid flow, shows no preferential current flow/rectification or problems with resistance between the electrodes. To test any effect that the lid material may have on the current, the base unit was sealed with an acetate film to mimic gen-1, figure s2. Also shown in figure 3d is example baseline current traces and noise during convection for various ionic strengths.

After the channel was sealed with the PDMS gasket and lid, the device was used as a resistive pulse sensor. 20μm particles were added to a sample reservoir and pushed

through the device using a range of flow rates. Figure 4a shows example current vs time trace, and the relationship between pulse frequency and flow rate, figure 4b. The pulse frequency, *J*, has linear relationships with flow rate, *ΔP*, and with concentration, C_s, (figure 4b,c), as predicted by equation 2, where the contribution from electrophoresis and electroosmosis is negligible given the high flow rates.[33]

$$J = C_s \Delta P. \qquad (2)$$

The blockade magnitudes and durations for figure 4b are shown in figure s3, illustrating that the flow rate does not change the magnitude of the signal, but does change the translocation times.
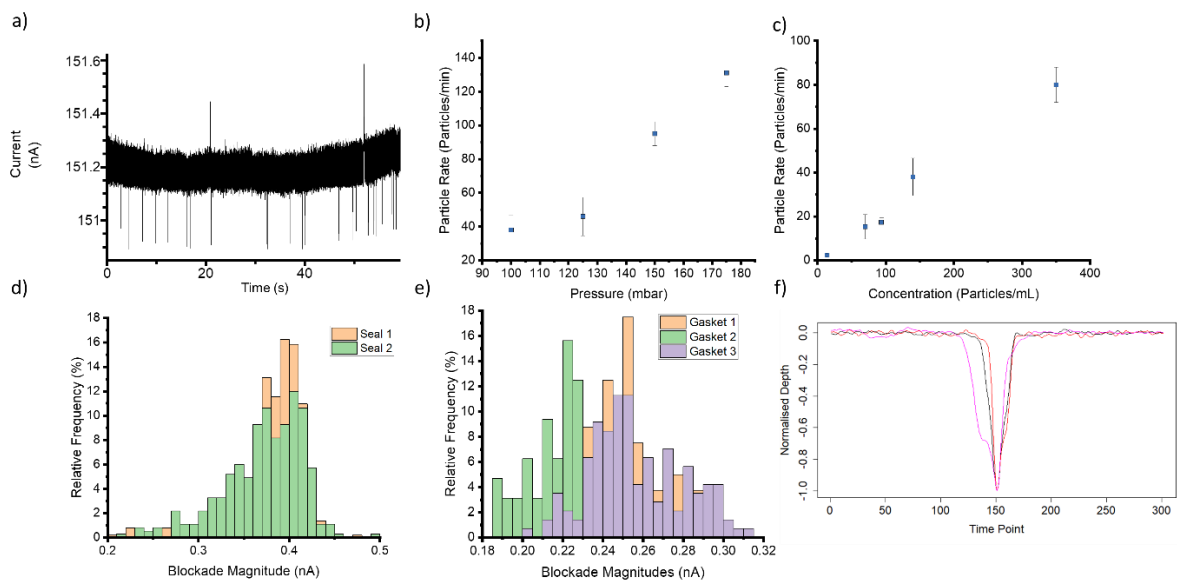

Figure 4 All examples were run on 0.25 mM KCl a) Example current trace from a ridge lid design, particles 20 × 10⁻⁶ m in diameter, 8.5 V. b) Particle count versus flow rate, particles 20 × 10⁻⁶ m in diameter, 8.5 V. c) Particle count versus concentration, particles 20 × 10⁻⁶ m in diameter, 8.5 V. d) Distribution of pulse magnitudes, particles 30 × 10⁻⁶ m in diameter, 5.64 V, before and after the same device and PDMS gasket was disassembled. e) Distribution of pulse magnitudes, particles 20 × 10⁻⁶ m in diameter, voltage = 7.5 V, using three different PDMS gaskets. f) Average pulse shape for each gasket in e, average of over > 60 particles

The same PDMS gasket could be reused 3 times before any leakages were observed, each time the components were placed together and the tension on the screws could be adjusted to match the baseline current. This was interpreted as producing a channel of similar dimensions. Example data sets from the same device and PDMS gasket taken apart and resealed are show in figure 4d. The device could remain sealed for four days without any deterioration in signal quality, figure s4, although it should be noted that on each day a calibration is needed to be run to quantify the analyte as there is some drift in the signal. An example of the reproducibility of the setup is also shown in figure 4e which shows the blockage distributions of 20μm particles using the same base and lid unit with different PDMS gaskets, with the average pulse shape shown in figure 4f for the three different assemblies. It is important to note that here the shape of the pulse reflects the internal shape of the sensing zone. Whilst we

hypothesised that the signal should be a rectangular pulse with a flat and consistent current during the translation event, the pulse shape indicates a different relationship. Similar effects were seen in the previous examples, and future work is needed to model the current and behaviour of the signal. We also note that the thickness of each PDMS gasket may vary, but by tightening the screws to match the base line current a consistent sensing zone could be produced each time. The pulse shape is also dependent upon the flow rate, as this effect the time within the channel, figure s5 shows the flow average pulse shape for spherical particles across a range of flow rates.

Changing the volume of the sensing zones allows the sensitivity of the RPS to be varied. An example of this is shown in figure 5a, where upon tightening the screws the blockage magnitude of the same sized particles increases with increasing screw tension. With this ability the same device, printed with an initial channel dimensions of 100x100x500 μm could measure particles from 2 to 30 μm figure 5b-e. This simple configuration enables an enhanced dynamic range on a single set of reusable components.
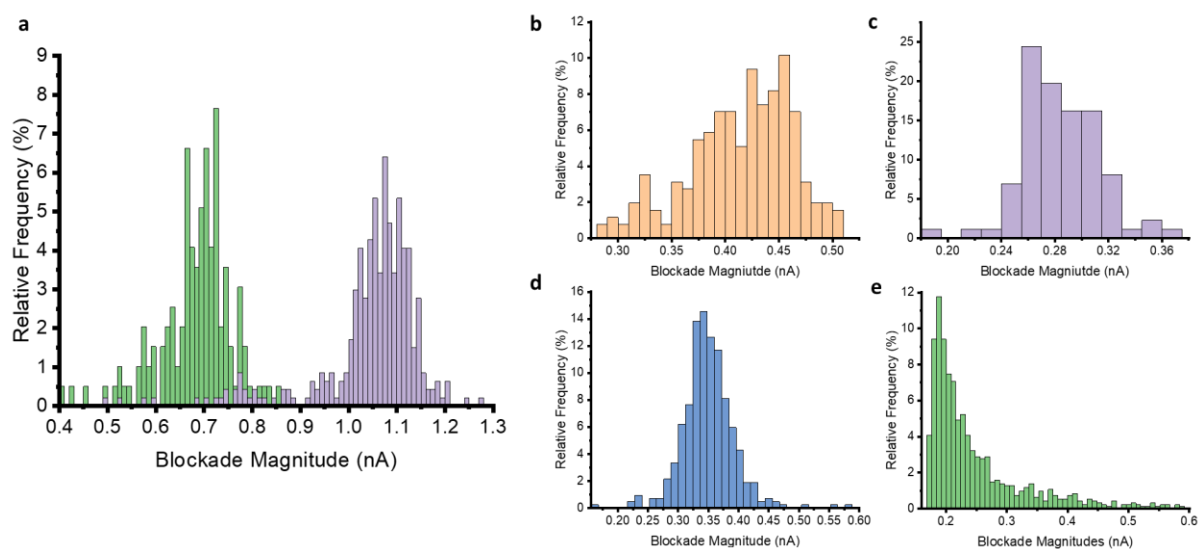

Figure 5 a) Blockade distributions for 30 × 10^{-6} m in diameter particles Voltage = 5.64 V, 0.25 mM KCl, using two different (low – green, high – purple) screw tensions. b) As a control, acetate tape (Gen-1) was used to seal the device. 30 × 10^{-6} m in diameter particles Voltage = 5.64 V, 0.25 mM KCl. Increasing the tension on the screws allows the RPS to measure smaller particles. c) 20 × 10^{-6} m in diameter particles Voltage = 8.5 V, 0.25 mM KCl , d) 10 × 10^{-6} m in diameter particles Voltage = 0.6 V, 100 mM KCl. e) 2 × 10^{-6} m in diameter particles Voltage = 1 V, 100 mM KCl.

The device was designed to screen environmental and food samples for contamination. An emerging threat to the global environment is that of microplastics, thus a first test was inspired by a recent publication. Hernandez and co-workers found that certain tea bags shed billions of plastic microparticles during their use. Follow their published protocol[34], we placed the bags into hot water for 5 mins, and passed the solution through our sensor. Within seconds, particles could be observed translocating the device, figure 6a. Using a particle of known size and concentration we calculated the average size to be 21.9 μm at 6.52 x 10^3 particles/ mL. We acknowledge that unlike in

the previous study we cannot be counting the entire particle size range and the number of nanoplastics are not included in this value. Teabags from several manufacturers were tested, and the total number of particles shed from one teabag was as high as 6.52×10^4, table s1. The presence of the particles was consistent across several tea manufactures, see figure s5, and analysis via SEM confirmed the particles were carbon based, figure s5. Varying the ionic strength of the liquid produced interesting effects, figure 6b. At lower ionic strengths, the pulse direction inverted and conductive pulses are prominently recorded. The inversion of the pulse could be caused by two factors, the first is that the polymers may contain a higher concentration of ions, making them "conductive" relative to the surrounding liquid; similar effects have been seen in hydrogels.[35] Alternatively, the high surface area seen in the SEM figure s5, combined with the lower ionic strength and a larger double layer, could result in a dense ion cloud around each particle that increase the conductivity of the liquid during each translocation. When the same polymer purchased with a smooth surface (figure s5b), was placed into the device, only resistive pulses were recorded even at low ionic strengths. Porous silica particles (figure s5c) found within toothpastes also produced predominantly conductive pulses at lower ionic strengths, table s2. Whilst the conductive pulse gives an indication of a change in physical properties, the lack or suitable calibrants makes it harder to size the particles using conductive pulses. For a fully automated screening device, confirmation of the chemical nature of the particles may require additional sensors embedded into the channels and is the scope of future work. However, the pulse direction may give an early indication of manmade particles.

Within oceans, counting plastics in the presence of biological particles is challenging. The results in figure 6, however, suggest that bacteria and algae particles, which have fairly smooth surfaces, should also give resistive pulses. This is confirmed within the data shown in Figure 6c and d. Here a series of data collected for algae particles across a range of ionic strengths is presented, and optical images for the algae are shown in figure s9. Figure 6 demonstrates that the algae always produce resistive pulses across all ionic strengths. This interesting observation may allow scientist to rapidly screen samples for the presence of plastics.
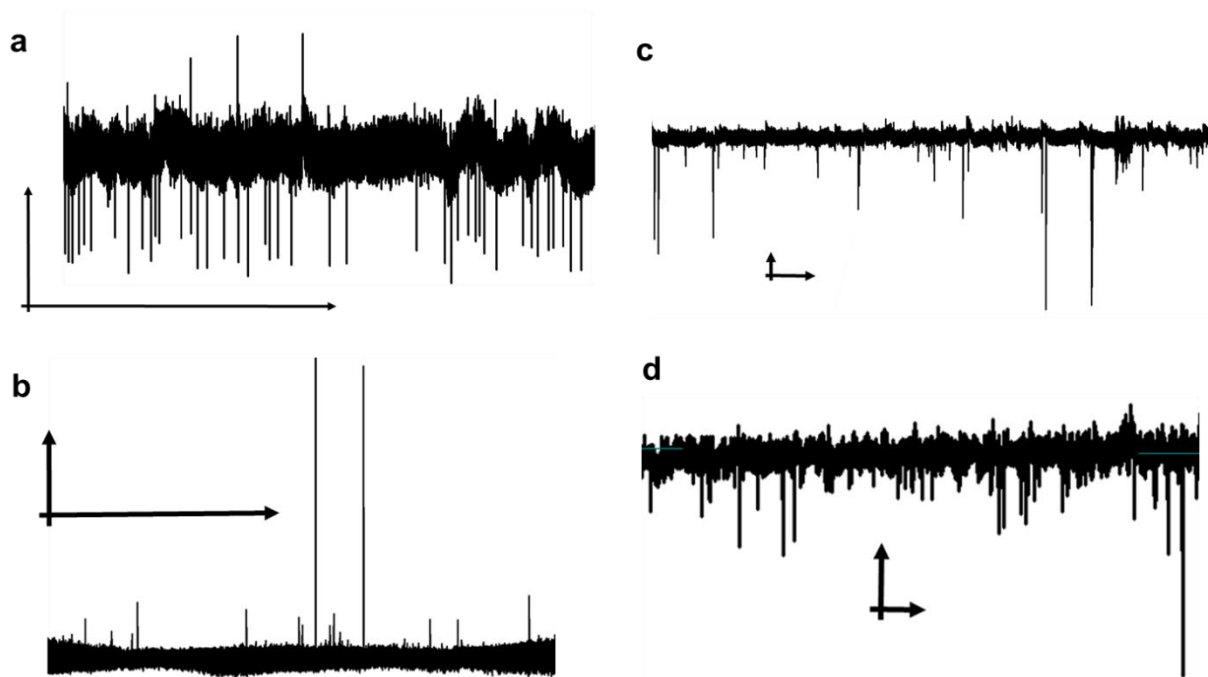
Figure 6 a) Microplastic particles run in 50 mM KCl, voltage, 0.4 V, b) Microplastic particles run in 0.25 mM KCl, 7.5 V c) Algae particles run in 50 mM KCl, 0.7 V, and d) 0.25 mM KCl 7 V. In all images scale bar is x = 10 sec. y = 0.5 nA.

Diatoms and algae are known to come in a variety of shapes depending upon the strain. Thus, a description of particle shape may help with the identification. Here we placed a rod-shaped algae (*Navicula ramosissima*) and some spherical algae (*Aurantiochytrium Mangrovei)* through the device. We have previously shown how the shape of a particle can be inferred from the shape of the pulse it generates.[15] Figure 7 shows the average depth-normalised pulse shapes for the two algae strains and their corresponding calibration bead runs. In order to quantify the differences between the pulses arising from algae and calibrants, the pulses were approximated by splines and the spline coefficients compared using a modelling method previously reported.[15] For these models the splines 5 (just before pulse minimum),10 and 11 (around the second peak in each pulse) were used, as they showed the greatest differences between the algae and calibrants. See figure S10 for each of the splines. For each type of algae, the model and device were calibrated against a sphere run under the same assembly. When comparing the calibrants to the algae, the model was able to correctly identify 87% of algae spheres and 86% of algae rods. This signifies that most of the algae can be identified against a spherical calibrant, see figure S11 for ROC graphs and result table S3. For comparison, when two runs of calibration spheres were run under the same assembly, the model correctly identified the run for only 66% of the spheres, which is close to the random 50% correct classification expected when pulses from two runs are identical. A surprising outcome of the data sets was the ability to identify spherical algae. Whilst their general shape should be similar to the calibrants, the algae have a flexible surface which may be deformed within the fluidic system. The deformation of biological particles has been explored for cells and

exosomes,[14,35,36] and here the same feature may help differentiate the biological particle from manmade ones. This establishes that the device can be used for shape analysis, and this is likely to improve with an optimised run method and model. A second unexpected and favourable outcome from the analysis was that the device was capable of shape analysis across multiple uses, e.g. days and assemblies, as long as it was calibrated each time; this is in contrast to the current commercial system that the model was originally developed for, which lost the ability to detect shape permanently after a much shorter period of use. The flow rate used to count the algae also affects the quality of the pulse shape information; as shown in figure 7b, the shape of the pulses from the two strains converge at higher flow rates. Whilst higher sampling frequencies may overcome this in future designs, this was beyond the scope of the current work.
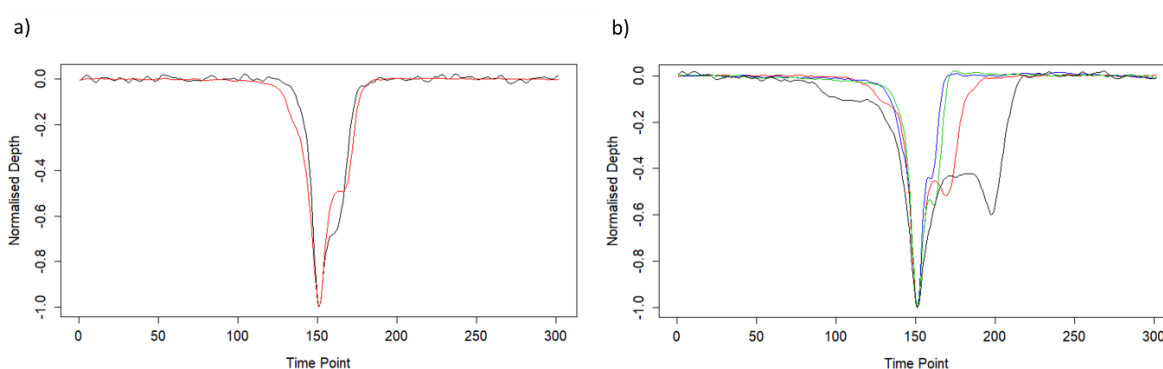

Figure 7 a) average pulse shapes of the spherical algae (black) to the rod shape algae (red), b) The average pulse shape for the rod algae across pressures, 50 mbar (black), 100 mbar (red), 125 mbar (green) and 150 mbar (blue).

Conclusions

In conclusion we have demonstrated a tuneable microfluidic RPS device with a reusable lid and base that allows the dimensions of the pore to be tuned in real time to the dimensions of the analyte. The device was able to detect particles as small as 2 microns in diameter; representing a ten-fold improvement in sensitivity on the previous generation of the device, which was limited by the resolution of the 3D printer. The device has been fully characterised including the effects of concentration, pressure and reassembling the device. The lowest concentration detected by the device was 14 particles per mL at a pressure of 100 mbar. The device was then tested with real world cases including the detection of microplastics in tea, where it was discovered that the plastics response to changing electrolyte concentration can be indicative of the material's porosity. The average size and concentration from one manufacture of teabag was determined to be 21.9 μm and 6.52×10^4 particles per mL. The device was also able to differentiate between two different shapes of algae in comparison to a calibration sphere, demonstrating that the device can discriminate an analyte on the basis of shape, an area we hope to develop further in the future.

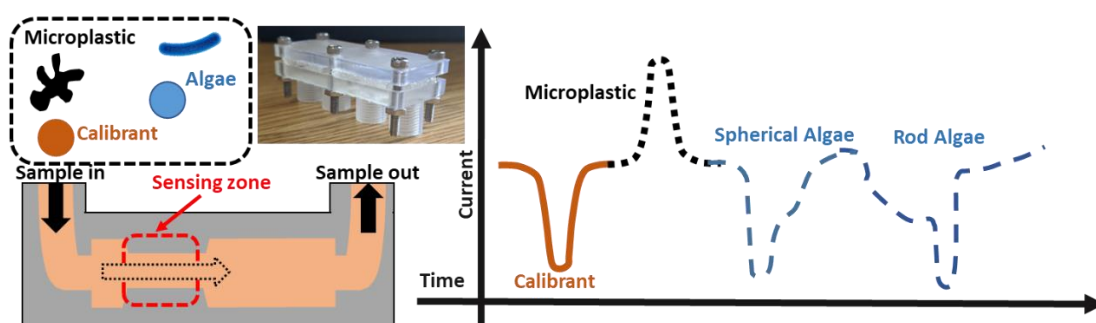**Supporting Information Available**

Supporting Information Available: The following files are available free of charge. Illustration of the design of the model, electric potential and field lines. Images of the RPS created with varying channel sizes, example pulses and signal versus flow rate for multiple devices. This material is available free of charge *via* the internet at http://pubs.acs.org

References

1   X. He, Y.-L. Liu, A. Conklin, J. Westrick, L. K. Weavers, D. D. Dionysiou, J. J. Lenhart, P. J. Mouser, D. Szlag and H. W. Walker, *Harmful Algae*, 2016, **54**, 174–193.

2   T. L. Richardson, E. Lawrenz, J. L. Pinckney, R. C. Guajardo, E. A. Walker, H. W. Paerl and H. L. MacIntyre, *Water Res.*, 2010, **44**, 2461–2472.

3   N. McQuaid, A. Zamyadi, M. Prévost, D. F. Bird and S. Dorner, *J. Environ. Monit.*, 2011, **13**, 455–463.

4   R. H. Becker, M. I. Sultan, G. L. Boyer, M. R. Twiss and E. Konopko, *J. Great Lakes Res.*, 2009, **35**, 447–453.

5   W. Zhang, Y. Hu, G. Choi, S. Liang, M. Liu and W. Guan, *Sensors Actuators B Chem.*, 2019, **296**, 126615.

6   Z. Song, M. Li, B. Li, Y. Yan and Y. Song, *Electrophoresis*, 2019, **40**, 897–905.

7   T. Zhou, Y. Song, Y. Yuan and D. Li, *Anal. Chim. Acta*, 2019, **1052**, 113–123.

8   J. Sun, Y. Kang, E. M. Boczko and X. Jiang, *Electroanalysis*, 2013, **25**, 1023–1028.

9   N. Khodaparastasgarabad, A. Mohebbi and C. Falamaki, *Microsyst. Technol.*, 2019, **25**, 3643–3653.

10   C. Bernabini, D. Holmes and H. Morgan, *Lab Chip*, 2011, **11**, 407–412.

11   R. Vogel, G. Willmott, D. Kozak, G. S. Roberts, W. Anderson, L. Groenewegen, B. Glossop, A. Barnett, A. Turner and M. Trau, *Anal. Chem.*, 2011, **83**, 3499–3506.

12   E. Weatherall, P. Hauer, R. Vogel and G. R. Willmott, *Anal. Chem.*, 2016, acs.analchem.6b01818.

13   A. D. Grabarek, D. Weinbuch, W. Jiskoot and A. Hawe, *J. Pharm. Sci.*, 2019, **108**, 563–573.

14   P. Hinkle, T. M. Westerhof, Y. Qiu, D. J. Mallin, M. L. Wallace, E. L. Nelson, P. Taborek and Z. S. Siwy, *Sci. Rep.*, 2017, **7**, 10173.

15   R. Maugi, P. Hauer, J. Bowen, E. Ashman, E. Hunsicker and M. Platt, *Nanoscale*, 2020, **12**, 262–270.

16   E. L. C. J. Blundell, R. Vogel and M. Platt, *Langmuir*, 2016, **32**, 1082–1090.

17   D. Kozak, W. Anderson and M. Trau, *Chem. Lett.*, 2012, **41**, 1134–1136.

18   Y. Song, H. Zhang, C. H. Chon, S. Chen, X. Pan and D. Li, *Anal. Chim. Acta*, 2010, **681**, 82–86.

19   Y. Song, J. Wang, J. Yang, Y. Wu, N. Li, N. Gong, X. Pan, Y. Sun and D. Li, *Instrum. Sci. Technol.*, 2012, **40**, 305–315.

20   I. Heaton and M. Platt, *Anal. Chem.*, 2019, **91**, 11291–11296.

21   B. Gale, A. Jafek, C. Lambert, B. Goenner, H. Moghimifam, U. Nze and S. Kamarapu, *Inventions*, 2018, **3**, 60.

22   A. J. Capel, S. Edmondson, S. D. R. Christie, R. D. Goodridge, R. J. Bibb and M. Thurstans, *Lab Chip*, 2013, **13**, 4583.

23   N. Bhattacharjee, A. Urrios, S. Kang and A. Folch, *Lab Chip*, 2016, **16**, 1720–1742.

24   S. Waheed, J. M. Cabot, N. P. Macdonald, T. Lewis, R. M. Guijt, B. Paull and M. C. Breadmore, *Lab Chip*, 2016, **16**, 1993–2013.

25   H. Gong, B. P. Bickham, A. T. Woolley and G. P. Nordin, *Lab Chip*, 2017, **17**, 2899–2909.

26   K. G. Lee, K. J. Park, S. Seok, S. Shin, D. H. Kim, J. Y. Park, Y. S. Heo, S. J. Lee and T. J. Lee, *RSC Adv.*, 2014, **4**, 32876–32880.

27   F. Perrucci, V. Bertana, S. L. Marasso, G. Scordo, S. Ferrero, C. F. Pirri, M. Cocuzza, A. El-Tamer, U. Hinze, B. N. Chichkov, G. Canavese and L. Scaltrito, *Microelectron. Eng.*, 2018, **195**, 95–100.

28   B. C. Gross, J. L. Erkal, S. Y. Lockwood, C. Chen and D. M. Spence, *Anal. Chem.*, 2014, **86**, 3240–3253.

29   S. M. Hampson, M. Pollard, P. Hauer, H. Salway, S. D. R. Christie and M. Platt, *Anal. Chem.*, , DOI:10.1021/acs.analchem.8b05140.

30   L. A. Godwin, K. S. Deal, L. D. Hoepfner, L. A. Jackson and C. J. Easley, *Anal. Chim. Acta*, 2013, **758**, 101–107.

31 H. Gong, A. T. Woolley and G. P. Nordin, *Lab Chip*, 2016, **16**, 2450–2458.

32 J. Riordon, M. Mirzaei and M. Godin, *Lab Chip*, 2012, **12**, 3016.

33 E. L. C. J. Blundell, L. J. Mayne, E. R. Billinge and M. Platt, *Anal. Methods*, 2015, **7**, 7055–7066.

34 L. M. Hernandez, E. G. Xu, H. C. E. Larsson, R. Tahara, V. B. Maisuria and N. Tufenkji, *Environ. Sci. Technol.*, 2019, **53**, 12300–12310.

35 D. A. Holden, G. Hendrickson, L. A. Lyon and H. S. White, *J. Phys. Chem. C*, 2011, **115**, 2999–3004.

36 A. Darvish, G. Goyal, R. Aneja, R. V. K. Sundaram, K. Lee, C. W. Ahn, K.-B. Kim, P. M. Vlahovska and M. J. Kim, *Nanoscale*, 2016, **8**, 14420–14431.

TOC image